

Advances in collision detection and non-linear finite mixed element modelling for improved soft tissue simulation in craniomaxillofacial surgical planning

Shengzheng Wang^{1,2*}

Jie Yang¹

James C. Gee³

¹Department of Automation,
Shanghai Jiao Tong University,
Shanghai, 200240, People's Republic
of China

²Merchant Marine College, Shanghai
Maritime University, Shanghai,
200235, People's Republic of China

³Department of Radiology, University
of Pennsylvania, Philadelphia, PA
19104, USA

*Correspondence to:

Shengzheng Wang, Department of
Automation, Shanghai Jiao Tong
University, Shanghai, 200240,
People's Republic of China. E-mail:
szwang.smu@gmail.com

Abstract

Background There is a huge demand to develop a method for assisting surgeons in automatically predicting soft tissue deformation in terms of a bone-remodelling plan.

Methods This paper introduces several novel elements into a system for the simulation of postoperative facial appearances with respect to prespecified bone-remodelling plans. First, a new algorithm for efficient detection of collisions, using the signed distance field, is described. Next, the penalty method is applied to determine the contact load of bone on facial soft tissue. Finally, a non-linear finite mixed element model is developed to estimate the tissue deformation induced by the prescribed bone remodelling plan.

Results The performance of the proposed collision detection algorithm has been improved in memory requirements and computational efficiency compared with conventional methods. In addition, the methodology is evaluated over both synthetic and real data, with simulation performance averaging <0.5 mm pointwise error over the facial surface in six mid-face distraction osteotogenesis procedures.

Conclusions The experimental results support the novel methodological advancements in collision detection and biomechanical modelling proposed in this work. Copyright © 2009 John Wiley & Sons, Ltd.

Keywords collision detection; non-linear finite mixed element modelling; soft tissue deformation; craniomaxillofacial surgery

Introduction

Background

Craniomaxillofacial surgery is performed to restore a patient's face to an improved configuration through the repositioning of bones or cranioplasty, and thus the capacity to predict the realistic motion of the facial tissues is a huge demand for surgeons. It may not only improve communication between surgeons and patients but also help surgeons to optimize surgical planning. Currently, therefore, many craniomaxillofacial surgical planning systems (CSPSs) appear to be widely in use by surgeons in computing an optimal plan and training for the purpose of repeatedly practising surgical procedures.

Over the past two decades, many research efforts have been dedicated to modelling the behaviour of the soft tissue deformation. Early work focused

Accepted: 16 October 2009

mainly on facial animation, based on masses and springs (1,2). Subsequently, anatomy based facial tissue models were proposed and implemented using the finite element method. Koch (3) and Keeve (4) first used prism elements to construct the geometric model of the facial soft tissues. However, this method lacked the accuracy and reliability of the mesh generation due to the complexity of the facial soft tissues so that the later researchers used tetrahedron elements rather than prism elements to represent the geometric structures of the facial soft tissues. At the same time, the real-time simulation using elastic finite element modelling was implemented (5–8) and there was an early survey on real-time soft tissue simulation (9). Although these methods obtained realistic visual results, their models were not informed by rigorous tissue biomechanics, which affected the accuracy of their soft tissue deformation solutions. Much work has since followed that focuses on biomechanical modelling of the soft tissue deformation (10–15). Furthermore, some of these have validated the effectiveness of such models to improve the clinical performance of the CSPSs (16–20).

Nevertheless, there are many limitations in the previous methods. These limitations result from at least two aspects: (a) the boundary conditions of the biomechanical model, which affect the accuracy and reliability of the facial soft tissue deformation, must still be defined manually by measuring the displacements of the bones in terms of the bone-related planning developed by the surgeon. This process is both tedious (one must iterate through measuring and registering the repositioning of the bones) and challenging (the precise face configuration sought after may be difficult to obtain with this approach), due to the complexity of the anatomy of the face; (b) the facial soft tissues were modelled with uniform material properties without distinguishing between skin, muscles and fat, which resulted in a lack of accuracy regarding the soft tissue deformation. The difficulty of assigning different material properties for the skins and the internal tissues results from the limitations of the geometric description of the facial soft tissues. Conventional geometric description methods are based on uniform volumetric elements and uniform shape functions, which is inadequate to assign unique material properties for skin and internal tissues.

After careful discussions with surgeons, it is clear that the limitations of the previous methods must be addressed to better model the deformation of the facial soft tissues and automatically predict the soft tissue deformation in terms of a bone-related plan in the CSPS. In order to achieve this simulation, we first need to know when and where two geometrical objects (bones and soft tissues) intersect and penetrate each other with repositioning of the bones, how much the penetration depth and the contact force are, and then how the soft tissues deform after the movements of the bones. Investigation results show that collision detection is a promising means to address the problem of when and where the bones and the soft tissues will intersect each other. Furthermore, the ability to compute the penetration depth in the

collision detection is the fundamental prerequisite to predict the soft tissue deformation accurately. In this paper, therefore, an efficient collision detection algorithm based on a new three-dimensional (3D) signed distance field is proposed to automatically estimate the penetration depth and contact force after the moving of the bones, and an improved biomechanical model based on non-linear finite mixed elements is proposed to enhance the soft tissue behaviour in the simulation. However, since the anatomical structures of the face are highly complex, the effectiveness and reliability of the collision detection algorithm and the biomechanical model are challenging in the CSPS. Therefore, both collision detection and biomechanical model are two key problems for this simulation.

To summarize our point of view, four main steps must be fulfilled to complete this simulation. (a) 3D geometric models, including bone and soft tissue models, are reconstructed from CT datasets, and the signed distance field of the skull-model is generated following the proposed signed distance field algorithm. (b) Bone cuts (osteotomies) are modelled with the help of a craniofacial surgeon, and the required cut surfaces for defining the bone regions are interactively generated, following the anatomical structures; in this way the skull-remodelling plan and the moving paths of the bones are computed. (c) The bones move automatically following the moving path of the bone-related plan; when the collision occurs, the contact nodes and the penetration depth between the moved bones and the soft tissues are computed using the proposed collision detection algorithm, and thus the penalty force of the soft tissue model is computed in terms of the penetration depth of the contact nodes. (d) The geometrical model based on the mixed elements and the boundary conditions serve as inputs for our simulator, and the proposed non-linear finite mixed-element method based on the hyperelastic material model is used to model the behaviour of the facial soft tissue and predict the new facial appearance.

Related work

Deformable continuous collision detection has been studied widely with the development of surgical simulation, robotics and games. Some methods based on bounding volume hierarchies (BVHs) or spatial subdivision are successfully applied to the detection of the contact between the surgical tool and an organ in the surgical simulation (21–24). However, for the craniofacial surgical simulation presented in this work, collision detection is not simply to detect the touch of objects. Instead, precise collision information, e.g. penetration depth and normals, is required for this simulation. Furthermore, intersection regions between the bones and the soft tissues are generally large. Therefore, the methods that have been widely used in the surgical simulation are not appropriate for this work, and an effective collision detection algorithm is highly desired. Fortunately, the distance fields, free from

these limitations, can be applied in collision detection and the estimation of the penetration depth and normals needed for the biomechanical model of the soft tissues is extremely fast and independent of the geometric complexity of the object (23). Therefore, a collision detection algorithm based on distance field can help to achieve efficiently collision detection between the bones (rigid objects) and the soft tissues (deformable objects).

The distance field is an effective representation of shape and has a wide range of applications, e.g. collision detection, motion planning and visualization for computer graphics. In collision detection, deformed distance fields were used to estimate the penetration depth of elastic polyhedral objects (25). Another method involves the partial distance field (26). It is suitable for detecting the contact between rigid objects and highly deformable objects. However, this method used uniform grid data structures, resulting in huge memory requirements. Frisken *et al.* (27) proposed the adaptive distance field technique. Their contribution is to reduce memory requirements and represent complex shape in diverse scales. However, this method increased the cost of more complex storage and retrieval. These drawbacks hamper the distance field from being applied in collision detection. Therefore the efficient computation of the distance field for a given surface representation is still a research topic. In this work, we describe an efficient method for computing the signed distance field by combining Fuhrmann *et al.*'s algorithm and the adaptive sampling method.

The remainder of the paper is organized as follows. The next section presents materials and methods, consisting of the collision detection algorithm and the simulation of soft tissue deformation. Then follow the experimental results, including performance evaluation and discussion. The final section reports our conclusions and future work.

Materials and Methods

System overview

We developed a CSPA for assisting surgeons in automatically computing an optimal surgical plan. It integrated a set of functions, including craniofacial soft tissue segmentation, geometrical model generation, bone-related planning and soft tissue deformation prediction. Figure 1 shows the framework of the whole system, and we mainly focus on the implementation of soft tissue deformation prediction based on collision detection.

Collision detection

3D signed distance field

For a solid S , the distance field of the corresponding surface ∂S can be defined as a scalar function, $D:R^3 \rightarrow R$, and thus the unsigned distance function generates the

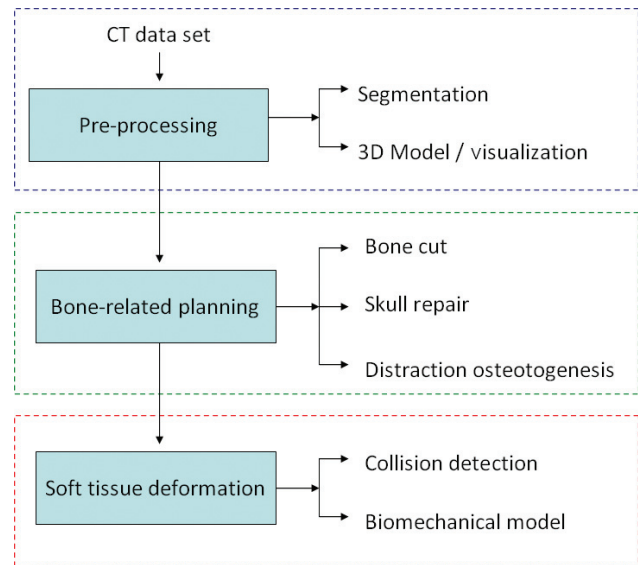


Figure 1. System framework

distance from a point \mathbf{p} to the closest point in the surface ∂S , as follows:

$$D_s(\mathbf{p}) = \inf_{\mathbf{q} \in \partial S} \|\mathbf{p} - \mathbf{q}\|, \quad \forall \mathbf{p} \in R^3 \quad (0.1)$$

Here, the distance field D defines a surface as the zero level set, that is $\partial S = \{\mathbf{p} | D(\mathbf{p}) = 0\}$. The signed distance function can be defined as:

$$D_s(\mathbf{p}) = \text{sgn}(\mathbf{p}) \cdot \inf_{\mathbf{q} \in \partial S} \|\mathbf{p} - \mathbf{q}\|, \quad \forall \mathbf{p} \in R^3 \quad (0.2)$$

where $\text{sgn}(\mathbf{p}) = \begin{cases} -1 & \text{if } \mathbf{p} \in S \\ 1 & \text{otherwise} \end{cases}$. The sign is used to denote whether a point is inside or outside S .

In this work, an efficient signed distance field algorithm is designed by combining the partial distance field algorithm (26) and the adaptive sampling algorithm (27). It can generate a signed distance field for the geometry with orientated triangle meshes, and does not require a closed and two-manifold surface. The algorithm that is used to generate a signed distance field for triangular geometrical model is summarized as follows (see algorithm 1):

1. For each triangle of the surface of the geometrical model, a prism is generated by moving its vertices along the surface normal by an amount of ζ in negative and positive directions (ζ is the assumed thickness of the distance field), as shown in Figure 2.
2. For each prism generated in step 1, the axis-aligned bounding box (AABB) enclosing this prism is determined, as shown in Figure 2.
3. For all grid points inside the corresponding bounding volume, the distances to the triangle of the surface are computed, and the signs of the distance values are determined by the sign of the angle-weighted pseudo-normal. If the calculated absolute value is less than the

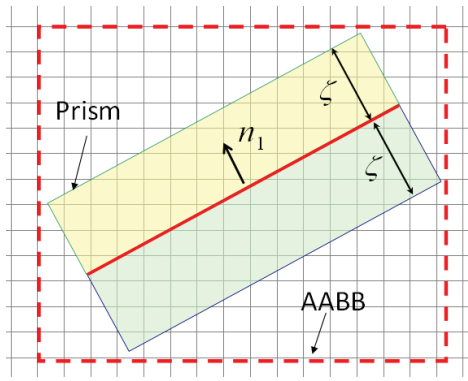


Figure 2. Prism of a triangle mesh and the AABB of the prism

current value of the distance field, the current value is set to a new value.

4. A hierarchical octree is constructed to organize the Cartesian grid points of the distance field, and subsequently an adaptive distance field is generated using an adaptive, detail-directed sampling method.

Algorithm 1; signed distance field computation

```

Require: triangles  $\Sigma$  of the surface with
surface normal  $\vec{n}$ , Cartesian grid  $\Omega$ 
Output: distance field  $\psi$ 
Initialization:  $\psi \leftarrow +\infty$ 
for: all  $\Delta \in \Sigma$  do
 $P \leftarrow \text{ComputePrism}(t, \vec{n}, \zeta)$ ;
 $B \leftarrow \text{ComputeAABB}(P)$ ;
for: all  $p \in B \cap \Omega$  do
 $d \leftarrow ||p - c|| \cdot \vec{n}$ ;
if  $p \notin \text{VoronoiRegion}(R_0)$  then
if  $p \in \text{VoronoiRegion}(R_1 | R_2 | R_3)$  then
 $d \leftarrow ||p - c|| \cdot \text{sgn}(\vec{n}_v \cdot \vec{r})$ ;
else
 $d \leftarrow ||p - c|| \cdot \text{sgn}(\vec{n}_e \cdot \vec{r})$ ;
end if
end if
 $d \leftarrow \min(\text{abs}(d), \text{abs}(\psi(p)))$ 
end for
end for
octree  $\leftarrow \text{GenerateOctree}(\Omega)$ 
AdaptiveSample(octree, error_tolerance)

```

In the above algorithm, steps 1 and 2 are straightforward, while steps 3 and 4 relate to two key problems, which are the sign computation of the distance value and the generation of the adaptive distance field. We describe efficient methods to address these two problems in this section.

For a given point p , the minimum distance from p to a triangle mesh can be calculated using the Voronoi regions of the features of the triangle, as shown in Figure 3. However, if the sign which determines whether a point is inside or not simply results from the sign of the inner

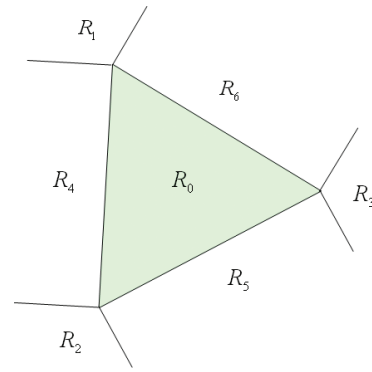
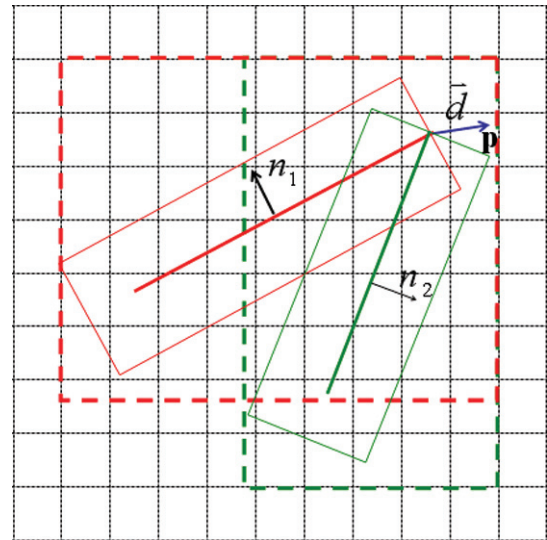
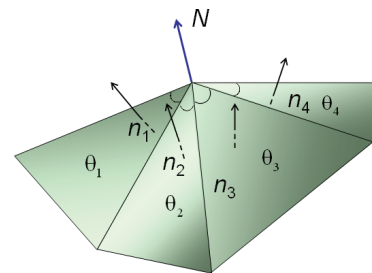


Figure 3. Voronoi regions of the features of the triangle

Figure 4. Mesh feature closest to p is a vertex of the triangle or a point at the edge of the triangleFigure 5. Angle weighted pseudo-normal N

product of the face normal and the direction vector (from point p to the closest point c on the surface), which is presented by Fuhrmann *et al.* (26), it does not work in many cases because in some cases the closest feature is a vertex or an edge; there is the same distance to two or more triangles but the dot product of $\vec{d} \cdot \vec{n}_1$ and $\vec{d} \cdot \vec{n}_2$ have different signs, as shown in Figure 4.

In this study, therefore, the angle-weighted pseudo-normal, which is guaranteed to have a positive dot product with the direction vector whenever the point is outside and negative whenever the point is inside (28), is employed to address this problem. As shown in Figure 5, for a given

vertex \mathbf{v} , the angle-weighted pseudo-normal is defined as:

$$\vec{N}_v = \frac{\sum \vec{n}_i \theta_i}{\|\sum \vec{n}_i \theta_i\|} \quad (0.3)$$

where $\{\theta_1, \theta_2, \theta_3, \dots\}$ are the incident angles of point \mathbf{c} , and $\{\vec{n}_1, \vec{n}_2, \vec{n}_3, \dots\}$ are the normals of the incident faces.

Since we are only interested in the sign, the normalization can be omitted and rewritten as:

$$\vec{N}_v = \sum \vec{n}_i \theta_i \quad (0.4)$$

which is conducive to improving computational efficiency.

In addition, for a given edge \mathbf{e} , the pseudo-normal is straight defined as

$$\vec{N}_e = \sum \vec{n}_i \quad (0.5)$$

Let there be a given grid point \mathbf{p} , the distance to the triangle mesh is:

$$d = \inf_{\mathbf{x} \in M} \|\mathbf{p} - \mathbf{x}\| \quad (0.6)$$

and assume that \mathbf{c} is a closest point in the triangle mesh M , so that the distance is:

$$d = \|\mathbf{p} - \mathbf{c}\| \quad (0.7)$$

and the direction vector is $\mathbf{r} = \mathbf{p} - \mathbf{c}$. Thus, the sign of the distance value is given by:

$$s_d = \text{sgn}(\vec{N}_v \cdot \vec{r}) \quad \text{or} \quad s_d = \text{sgn}(\vec{N}_e \cdot \vec{r}) \quad (0.8)$$

which means that $s_d > 0$ if \mathbf{p} is outside the surface, and $s_d < 0$ if \mathbf{p} is inside.

A signed distance field generated in steps 1–3 is based on a uniform 3D grid data structure. This data structure is easy to implement and the distance queries can be computed in constant time, but the drawbacks of this data structure are obvious, e.g. huge memory requirements and limited resolutions. In order to overcome these drawbacks, an adaptive, detail-directed sampling approach is used to optimize the distance field, i.e. high sampling rates are applied in the field containing fine details, and low sampling rates in the smooth field. In addition, the integration of detail-orientated sampling and the use of a spatial hierarchy for data storage makes it possible for adaptive distance field to represent complex shapes with arbitrary precision while still maintaining efficient processing.

In order to perform the adaptive sampling approach, an octree-based hierarchical data structure is used to store the sampled data, so as to process the sample data more efficiently. First, an octree is constructed to store the regularly sampled distance field generated in step 3, and then the bottom-up approach is used to recursively unite leaf cells within a specified error tolerance. The error tolerance is a predicate to controlling the coalescence or subdivision of the octree-based hierarchical data structure. We use a simple predicate

that compares the distance value of a cell's corner, computed using the distance function to the distance reconstructed from the sampled values of its parent cells, using trilinear interpolation. Therefore, the error tolerance is defined as the absolute difference between the computed and reconstructed distance values of a cell's corner. Specifically, a group of adjacent cells, starting with the smallest in the octree, are coalesced as long as none of them has child cells, and the sampled distance of the eight cells can be reconstructed from the sample values of their parent cells to a specified error tolerance. Upon considering all the cells for coalescing at a given level in the hierarchy, the group of cells at the next level is considered. The adaptive distance field generation is completed when the coalescence is finished at a given level or the root node is reached.

Collision detection and penetration depth computation

Collision detection between different objects is carried out pointwise when using a distance field. Vertices on the internal surface of the deformable object (the soft tissue model) are compared against the distance field of other objects (bones). A collision occurs if $D_s(\mathbf{p}) < 0$. An adaptive distance field stores distance values at cell vertices of an octree data structure and uses trilinear interpolation for reconstruction and gradient estimation.

However, as shown in Figure 6, the collision occurs between the deformable surface and the rigid object, but if only the vertices (v_i, v_j, v_k) of the surface were detected, collision would not occur. In order to avoid these artifacts, the barycentric coordinate O_{ijk} of the triangle is tested in the collision detection process.

Penalty force

We assume that the contact between the bones and the soft tissues is frictionless, and thus the contact force is normal to the surface. The normal is the partial derivative of a gap function g with respect to spatial coordinates. Thus, the contact force is:

$$\mathbf{f}_c = p_c \mathbf{n} = p_c \frac{\partial g(\mathbf{x})}{\partial \mathbf{x}} \quad (0.9)$$

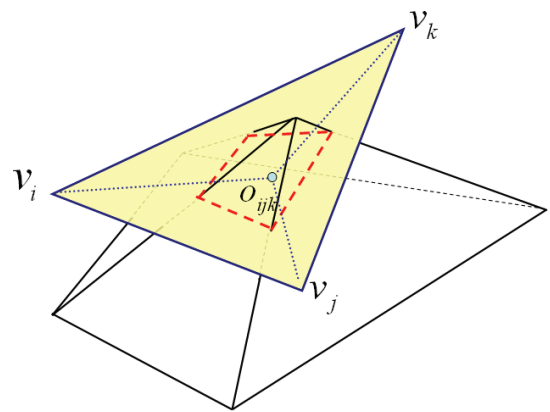


Figure 6. Barycentric coordinate O_{ijk} is detected to avoid artifacts

where p_c is contact pressure, which can be replaced with penalty $k_c g$ as:

$$\mathbf{f}_c = k_c g(\mathbf{x}) \frac{\partial g(\mathbf{x})}{\partial \mathbf{x}} \quad (0.10)$$

where k_c is a penalty constant.

Note that the contact force is the partial derivative of penalty-potential energy $\phi = k_c g^2/2$, i.e:

$$\frac{\partial \phi}{\partial \mathbf{x}} = \frac{\partial}{\partial \mathbf{x}} \left(\frac{1}{2} k_c g^2 \right) = k_c g(\mathbf{x}) \frac{\partial g(\mathbf{x})}{\partial \mathbf{x}} \quad (0.11)$$

In this paper, the penalty-potential energy is defined as a function of imposed displacements:

$$\phi(d) = k_c d^2 \quad (0.12)$$

The external contact force is therefore computed as follows:

$$\mathbf{F}_a^{\text{ext}} = \int_{\partial V^{(e)}} \frac{\partial \phi}{\partial \mathbf{x}} N_a da \quad (0.13)$$

Simulation of soft tissue deformation

Geometry description of the mixed element

The skin and muscles cannot be easily modelled using the uniform element type, since they have different geometric structures and material properties. In order to better model the skin tissues and the internal tissues (muscles and fat); the skin tissues are discretized into prism elements and the internal tissues into tetrahedron elements, as shown in Figure 7. To construct the geometric model, the first step is to extract the skin and skull surfaces with a marching cubes algorithm from CT datasets and to optimize them with mesh algorithms (29,30). Then the external surfaces of the internal tissues are obtained by projecting the vertices of the skin surface medially along a direction normal to the surface by an amount ζ , the assumed thickness of the skin. Generally, ζ averages 1.5 mm. Thus, the skin tissues are discretized into a number of prism elements, as shown in Figure 7. At the same time, the internal tissues are discretized into a number of tetrahedron elements in terms of the external surface of the internal tissues, as shown in Figure 7.

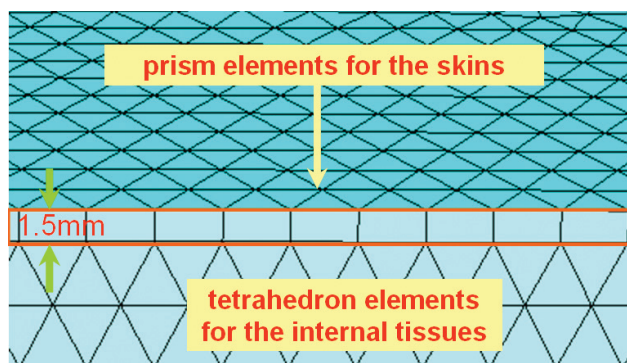


Figure 7. Geometric structures of the mixed-elements

In order to satisfy both the need for rendering smooth surfaces and the demand to conform to the underlying physics, the C^1 -continuous shape functions are expected at the facial surface and the C^0 -continuous shape functions in the interior elements. Simply, the C^1 -continuous shape functions can be designed for prism elements and the C^0 -continuous shape functions for tetrahedron elements. However, the prism elements and the tetrahedron elements cannot be assembled due to the discontinuity of the number of degrees of freedom between them. Therefore, special transition shape functions are necessary to combine the tetrahedron element with the prism elements.

For the tetrahedron elements, the linear shape functions are used to reduce the overall number of degrees of freedom of the system and are defined as:

$$N_i(\xi) = \xi_i, \quad i = 1, 2, 3, 4 \quad (0.14)$$

where ξ_i is the volume barycentric coordinates of the tetrahedral element.

Likewise, the linear shape functions are employed for the prism elements and defined as:

$$N^6(L_1, L_2, L_3, q) = [L_1(1-q) L_2(1-q) L_3(1-q) L_1 q L_2 q L_3 q] \quad (0.15)$$

where L_1, L_2 and L_3 define a barycentric surface coordinate system and q denotes the volumetric extension with $q = 0$ at the top surface and $q = 1$ at the bottom surface of the prism element.

In order to satisfy both aims mentioned above, the C^1 -continuous shape functions of the prism element are developed as an extension to the C^1 -continuous shape functions of the plate bending element. As shown in Figure 8, for a plate-bending element, the C^1 -continuous shape functions (see Appendix A for more details) are defined as:

$$\mathbf{N}^{9*} = \mathbf{N}^9 + [\phi_{23} \phi_{31} \phi_{12}](\mathbf{Y} - \mathbf{Z}) \quad (0.16)$$

where \mathbf{N}^9 is the basic Hermite-type interpolation functions of a triangular elements, ϕ_{23} , ϕ_{31} and ϕ_{12} are correcting functions, \mathbf{Y} is the average of the corresponding cross-boundary derivatives at the endpoints of each edge and \mathbf{Z} is cross-boundary derivatives at the edge midpoints.

Hence, the prismatic shape functions can be reformulated as:

$$\mathbf{N}^{12}(L_1 L_2 L_3 q) = [\mathbf{N}^{9*}(1-q) L_1 q L_2 q L_3 q] \quad (0.17)$$

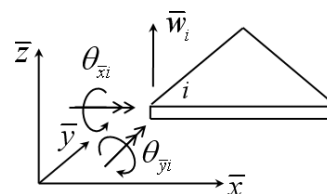


Figure 8. A plate-bending element with three nodes

Thus, the prism shape functions featuring C^1 -continuity at the facial surface are constructed, and the interior elements are left to be C^0 -continuous, as shown in Figure 9.

For a given point \mathbf{x} in the configuration, the displacement vector is defined as:

$$u(\mathbf{X}) = \sum_{i=1}^n N_i \mathbf{u}_i \quad (0.18)$$

where \mathbf{u}_i is the i th node's displacement, n is the number of nodal points and N_i are the shape functions.

Non-linear finite element method based on hyperelastic relationship

Soft tissues typically exhibit hyperelastic, anisotropic and viscoelastic behaviours (31). Nevertheless, due to the difficulty in considering all of the mentioned features, normally soft tissue-related problems have been simplified. Recently, the hyperelastic material models have been widely used to model soft tissues in the surgical simulation (15,17,32), but the effect of this depends on the choice of the strain energy density function and the corresponding constitutive parameters. In this study, therefore, the hyperelastic model was employed to model the facial soft tissues and the strain energy functions and the parameters were investigated.

A strain energy density function is a scalar valued function that relates the strain energy density of a material to the deformation gradient, and can be written as:

$$W = W(\mathbf{C}) \quad (0.19)$$

where \mathbf{C} is the right Cauchy–Green tensor, defined as $\mathbf{C} = \mathbf{F}^T \mathbf{F}$, \mathbf{F} , being the deformation gradient.

For an isotropic material, the deformation gradient can be expressed uniquely in terms of the principal stretches or the invariants of the left Cauchy–Green deformation tensor (\mathbf{B}) or right Cauchy–Green deformation tensor (\mathbf{C}), and we have:

$$W = \hat{W}(\lambda_1, \lambda_2, \lambda_3) = \bar{W}(I_1, I_2, I_3) \quad (0.20)$$

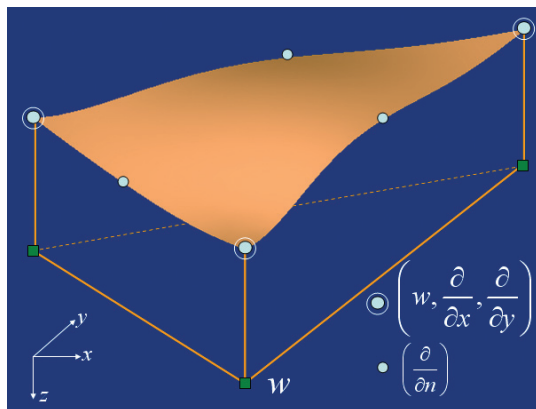


Figure 9. Prism elements with C^1 -continuous surface at the top and C^0 -continuity at the bottom plane

where invariants of \mathbf{C} are defined as:

$$I_1 = \text{tr}(\mathbf{C}) = \lambda_1^2 + \lambda_2^2 + \lambda_3^2$$

$$I_2 = \frac{1}{2}[(\text{tr}(\mathbf{C}))^2 - \text{tr}(\mathbf{C}^2)] = \lambda_1^2 \lambda_2^2 + \lambda_2^2 \lambda_3^2 + \lambda_3^2 \lambda_1^2 \text{ and}$$

$$I_3 = \det(\mathbf{C}) = \lambda_1^2 \lambda_2^2 \lambda_3^2, \lambda_i$$

and are the principal stretches.

To choose a suitable strain energy density function, we have assumed the soft tissue to be an incompressible, homogeneous and isotropic elastic material. The two-term Mooney–Rivlin equation is employed to represent the strain energy function, and is defined as:

$$\bar{W}(I_1, I_2, I_3) = C_{10}(I_1 - 3) + C_{01}(I_2 - 3) \quad (0.21)$$

where C_{10} and C_{01} are material constants.

The experimental stress–strain data are used to estimate the material constants. The coarse experimental data of the skin, muscles and fat can be found in (31,33), as shown in Figure 10. To find the material constants of the model, the curve was used in a least square curve-fitting procedure. Figure 11 shows the approximate results of different soft tissue. The estimated constitutive parameters employed in the hyperelastic model associated with the non-linear mechanical definition of the soft tissues are estimated and presented in Table 1.

Results and Discussion

We acquired datasets of six patients with mid-face craniofacial dystosis who underwent mid-face distraction

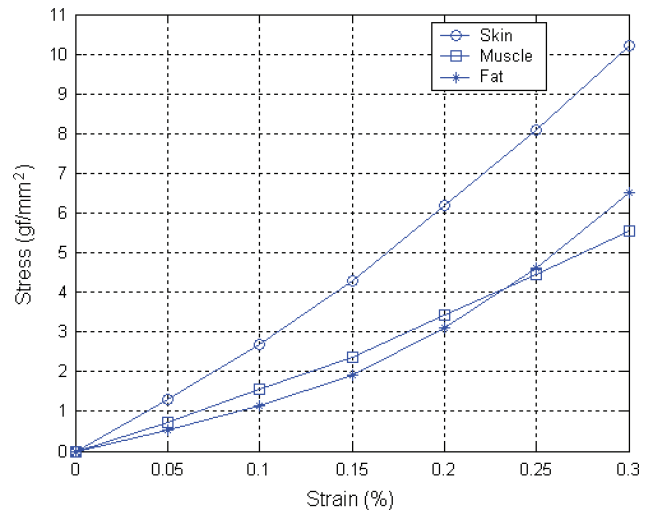


Figure 10. Strain–stress relationship of the soft tissues

Table 1. Hyperelastic material parameters of the soft tissues for Mooney–Rivlin model (gf/mm^2)

Type	D1	C10	C01
Skin	0.49	18.9834587	−15.4071649
Muscle	0.3	9.84540206	−7.74326281
Fat	0.49	16.6131140	−16.0126823

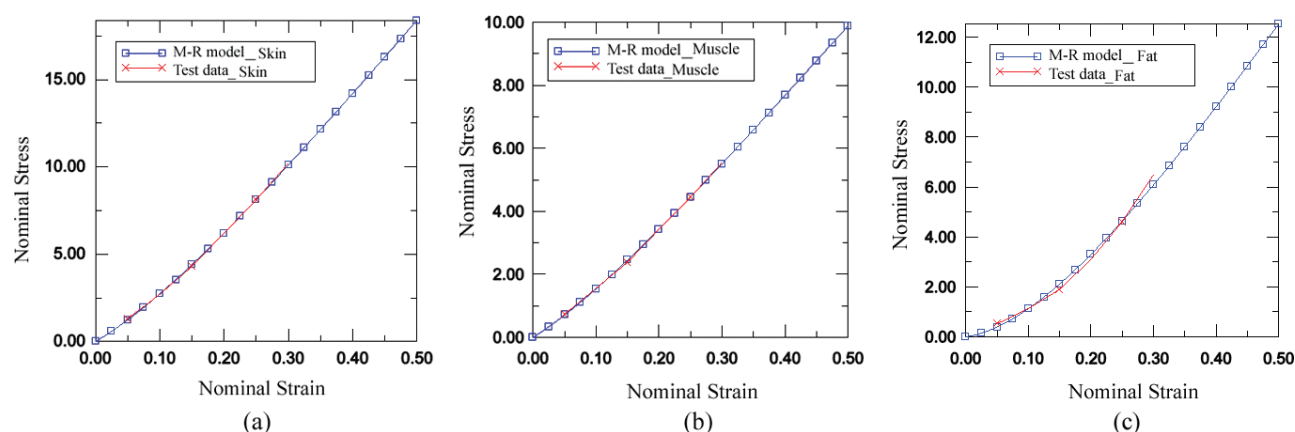


Figure 11. Material properties evaluation results: (a) the fitted curve of the M-R material model for skin; (b) the fitted curve for muscles; (c) the fitted curve for fat

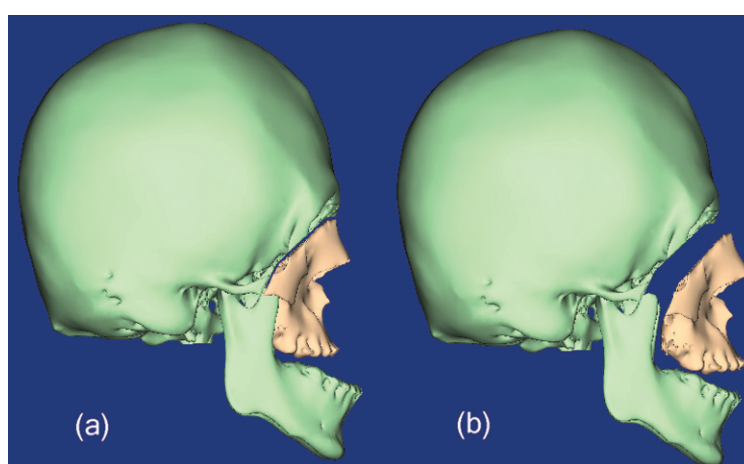


Figure 12. Repositioning of the bones: (a) the definition of osteotomies; (b) the movements of the bones

Table 2. The datasets of six patients

Patient No.	Displacements(mm)		Nprisms	Ntets	Time (s)
	Forward	Downward			
1	12.2	1.5	11 256	123 782	1093
2	8.5	1.2	12 967	129 569	1225
3	9.8	1.6	11 653	126 729	1186
4	6.8	0.8	14 051	130 856	1299
5	12.0	2.1	14 673	131 231	1325
6	7.8	1.8	13 872	130 092	1256
Average	9.52	1.50	13 079	128 710	1230

osteotogenesis using Le Fort III osteotomy. The objective was to simulate correction of the craniofacial dysostosis with mid-face distraction osteotogenesis. Table 2 summarizes the patient number, the moving planning of the mid-face, the number of the prism elements, the number of the tetrahedron elements of the geometrical model of the soft tissues and the time needed to calculate the penetration depth and solve the finite element model. All calculations were performed on a workstation with a Dual-Core AMD Opteron CPU 3.0 GHz, with 4 G of RAM and a NVIDIA Quadro FX 5500 GPU. As seen from Table 3, the forward average displacements of the bones are 9.52 mm

and the downward average displacements are 1.5 mm. Although the number of the prism and tetrahedron elements is very large, the average simulation time is ca. 20 min. Patient 1 in Table 3 is used to describe the implementation of the proposed method. Figure 12 shows the moving of the cut regions of the bones. Figure 13 shows the predicted results under different movements of the bones.

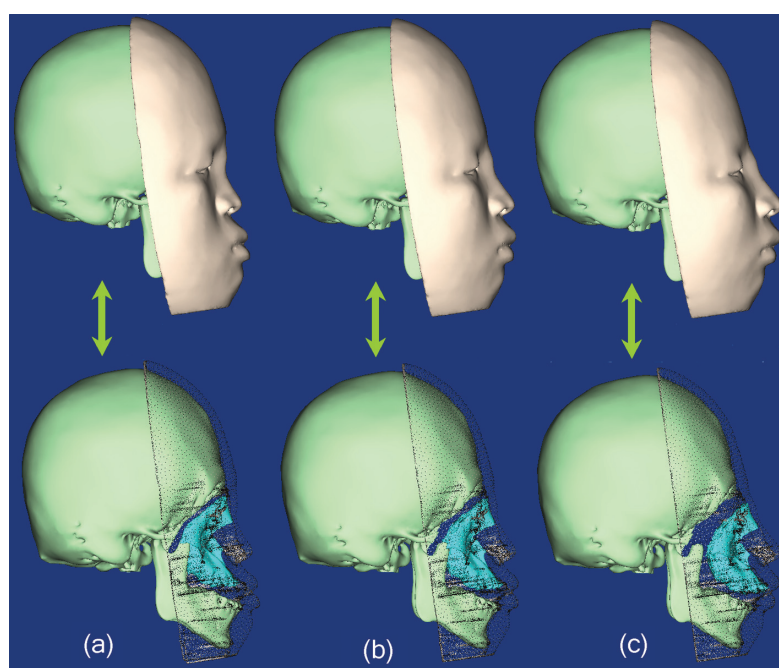
Performance evaluation

Collision detection

We have tested our distance field algorithm with a skull model (triangular meshes with 96,190 faces) at variable resolutions and error tolerances, and compared the proposed approach with the two conventional methods: the fast partial distance field computation method using uniform grid data structure (26), and the adaptive distance field technique (27). Table 3 summarizes the memory requirements and computational time at different grid resolutions or different error tolerances. In Table 3, the error tolerance is defined as the absolute difference between the computed and

Table 3. Performance comparison of distance field computation (triangles: 96, 190)

Resolution	Error tolerance	Fuhrmann <i>et al.</i> (26)		Friskin <i>et al.</i> (27)		Our algorithm	
		Memory (M)	Time (s)	Memory (M)	Time (s)	Memory (M)	Time (s)
128 × 128 × 128	1.0 × 10 ⁻³	8.4	3.12	3.2	11.78	2.9	4.26
128 × 128 × 128	1.0 × 10 ⁻⁵	8.4	3.12	7.5	33.52	6.6	12.43
256 × 256 × 256	1.0 × 10 ⁻³	67.1	13.15	12.9	65.54	11.5	16.75
256 × 256 × 256	1.0 × 10 ⁻⁵	67.1	13.15	19.7	107.39	16.1	18.12
256 × 256 × 256	1.0 × 10 ⁻⁶	67.1	13.15	46.8	239.60	42.7	23.82
512 × 512 × 512	1.0 × 10 ⁻⁶	536.9	60.62	99.5	965.83	95.1	68.15

**Figure 13.** Results of soft tissue deformation based on mixed-element modelling: (a) preoperative face configurations; (b) the predicted face configurations with the bones of the mid-face moving 6 mm forwards; (c) the predicted face configurations with the bones of the mid-face moving 12 mm forwards and 5 mm downwards (See movie in the Supporting information)

reconstructed distance values of a cell's corner. The memory requirements and computational time of the different algorithms are compared at different initial grid resolutions. The average memory requirements of our algorithm have been reduced by 60% against the uniform grid method (Fuhrmann *et al.*'s method). Although the average computational time of the distance field computation is slightly larger than Fuhrmann *et al.*'s method, the average computational time has been reduced by 77% against the adaptive distance field, since steps 1 and 2 in our algorithm (see algorithm 1) are used to eliminate large number of grid points.

Collision detection between different objects is carried out pointwise when using a distance field. We have performed the collision detection between the skull and the soft tissues during the moving of the bone models. The skull model has 96 190 triangle surface meshes, and the soft tissue model has 11 256 prism elements for the skin and 123 782 tetrahedron elements for the internal soft tissues. In the experiment, we fixed the grid resolution of the distance field as 256 × 256 × 256, and tested the

performance of the collision detection under different error tolerances. Figure 14 shows the collision detection time under different error tolerances. The specified error tolerance decreases from 1.0 × 10⁻⁵ to 1.0 × 10⁻⁶; the average increasing detection time is about 10 ms. As seen from Table 3 and Figure 14, we found that error tolerance is an important criterion in distance field computation and collision detection. A large error tolerance reduces the accuracy of the distance field. Instead, a small error tolerance increases the memory requirements and the computational time. Therefore, a suitable error tolerance needs to be specified in the experiments. Generally, we can obtain good performance when the error tolerance value is specified as 1.0 × 10⁻⁵ in the collision detection experiments.

Simulation of soft tissue deformation

The way to effectively measure the accuracy of the prediction is by comparing postoperative data with the predicted data (17,20). The following quantitative protocol was defined to evaluate the experimental results:

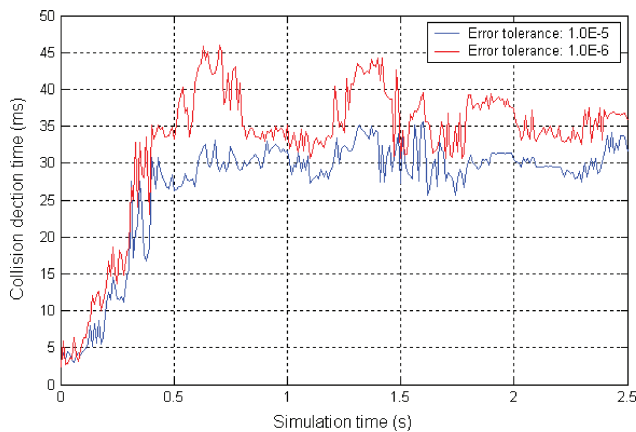


Figure 14. Performance comparison under different detection precisions

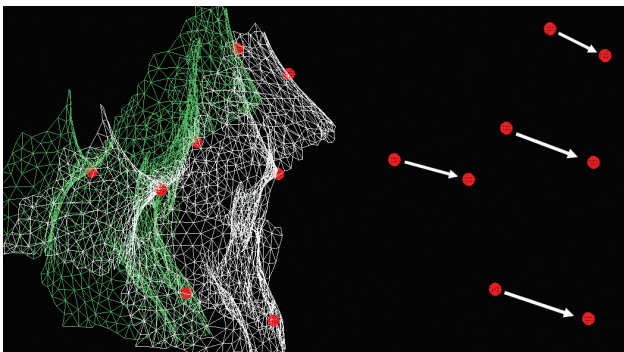


Figure 15. Registration of the preoperative and postoperative bone surfaces

1. After registration of the pre- and postoperative skull surfaces, the displacements of the cut bones are measured, as shown in Figure 15. Subsequently, the plan of the bone movements is obtained;
2. Following the bone-related planning, the boundary conditions are defined and serve as input for the simulator.
3. Simulating the resulting soft tissue deformation using the biomechanical model.
4. Evaluating the differences between the actual face configurations and the predicted face configurations quantitatively.

Quantitative validation implies measurement of the distances between corresponding points of the predicted and postoperative facial skin surfaces. For these measurements, the predicted and postoperative facial skin surfaces are first rigidly registered, based on an unaltered subvolume, and subsequently the distance between the two surfaces is determined. The distance map is computed using a signed Euclidean distance (17,34). All datasets, as shown in Table 3, were processed following the validation procedure described above. To improve the validation, the eye regions of each patient were manually selected and omitted during processing. Differences in these regions are mainly due to the opening or closing of the eyelids

during acquisition of the preoperative and postoperative CT scans.

Figure 16 shows the distance maps for each of the six patients. The colour map ranges between -3 mm and 3 mm, where a negative error means that the predicted skin surface lies behind the postoperative skin surface.

We compared four different computational strategies, consisting of a linear finite element model (FEM), a mass tensor model (MTM), a non-linear finite element model (NFEM) and the proposed method (NFM-EM). In FEM, MTM and NFEM, the soft tissues are modelled with uniform tetrahedral meshes and the interpolations between the mesh nodes are implemented by using a basic linear, C^0 continuous shape function for each tetrahedron. The MTM was introduced by Cotin (7).

Figure 17 shows the distance map results of the first case, using four different models. Figure 18 shows the statistical results of the average errors, the variance, the maximum errors and the distance errors ($L2 - Norm$) of the distance maps. The results show that the most accurate result is obtained by NFM-EM. The variance of the distance errors is the least in all methods, which means that NFM-EM is the most stable model. In addition, the average error is <0.5 mm and the accumulated distance errors ($L2 - Norm$) stay <30 mm.

Discussion

The proposed method is successfully demonstrated in a preliminary application to complex craniomaxillofacial surgery. The implementation develops a new biomechanical model, based on mixed-elements, that not only maintains the features of the finite volumetric element method but also provides C^1 continuous finite element surfaces. As a result, the soft tissues of the face are discretized into prismatic and tetrahedral elements. In this way, the different biomechanical characteristics of the skin and the internal tissues are effectively incorporated into the soft tissue model of the face, enabling the potential for significantly higher accuracy in the soft tissue simulation.

The conventional methods, MSM (1), MTM (20) and FEM (3), are homogeneous biomechanical models that do not incorporate tissue-specific behaviour, and Westermarck *et al.* (19) concluded that the net improvements of such inhomogeneous tissue models do not significantly influence the prediction quality in their experiments (19). However, the experimental results in this work (see Figures 17, 18) show that the differences between homogeneous material properties and non-homogeneous material properties are large. The main reasons are perhaps that they only used linear elastic materials, and differentiated between the muscles and the fat rather than the skin and the muscles. In fact, we found that the difference between the skin and the muscle is larger than that between the muscles and the fat.

For quantitative validation, the variance and the distance errors ($L2 - Norm$) are two significant evaluation

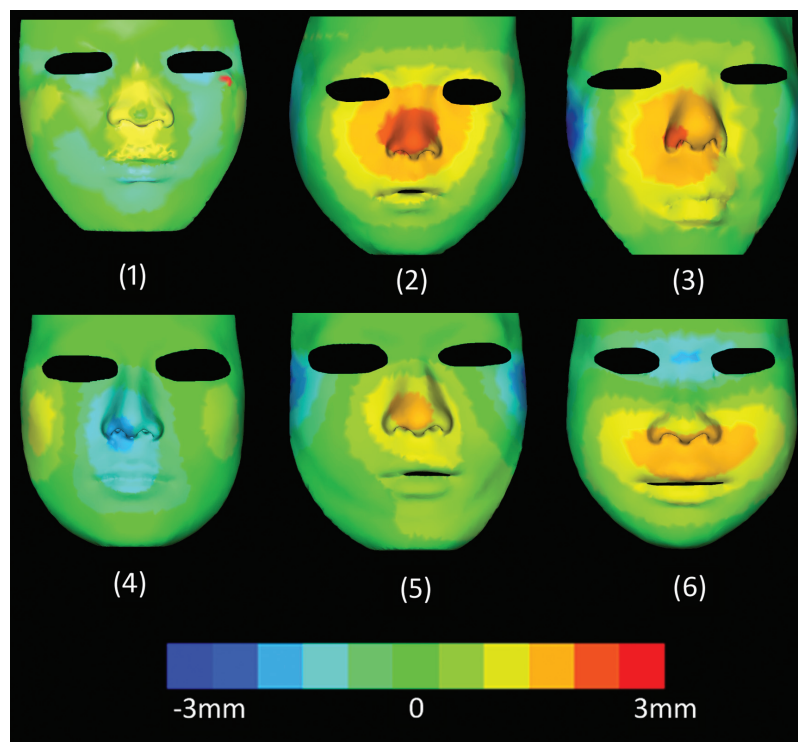


Figure 16. Distance map visualized by colour coding for the six patients

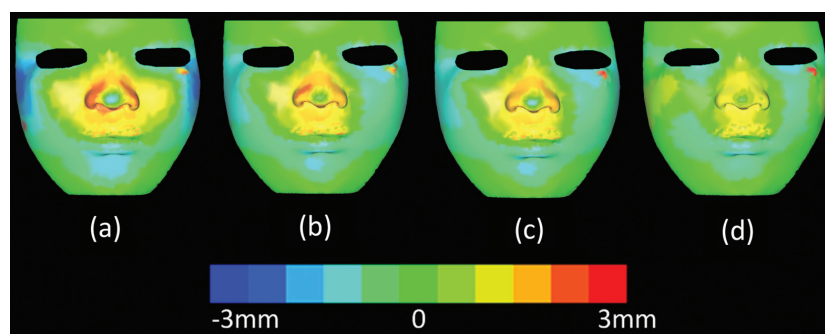


Figure 17. Four different computational models are used to predict the postoperative appearance of the first patient. Distance map between corresponding points of the predicted and postoperative facial appearance is visualized by colour coding: (a) linear finite element model (LFEM); (b) mass tensor model (MTM); (c) non-linear finite element model (NFEM); (d) the proposed method (NFM-EM)

criteria. The variance measures the distribution of the errors, and the L2 – Norm indicates the accuracy of the prediction. For the NFM-EM, the average or maximum error is not the least in all methods; however, the variance and the total distance error (L2 – Norm) are both the least, and the effect of the NFM-EM is the best, as shown in Figure 17.

In addition, since the non-linear finite element is much more sensitive to boundary conditions and material parameters, the definition of boundary conditions is a key factor for non-linear finite element model. However, it is difficult to define the boundary conditions for the facial soft tissue model using such conventional methods as manual measurement registration, due to the complexity of the facial geometric structures, which is another reason why many studies have concluded that the non-linear

finite element did not significantly enhance the accuracy of the soft tissue deformation. However, in this study we employed an accurate collision detection algorithm to estimate the penetration depth and the penalty force, which successfully define boundary conditions automatically. Therefore, the superior computational strategy of the boundary conditions presented in this paper has great significance in promoting the development of the soft tissue prediction systems based on bone-related planning. It not only helps us estimate the contact forces between the bones and the soft tissues automatically, but also improves the accuracy and the efficiency of the surgical planning system.

However, large errors occur in some quantitative validation results, due to an expression change in these experiments during acquisition of the preoperative and

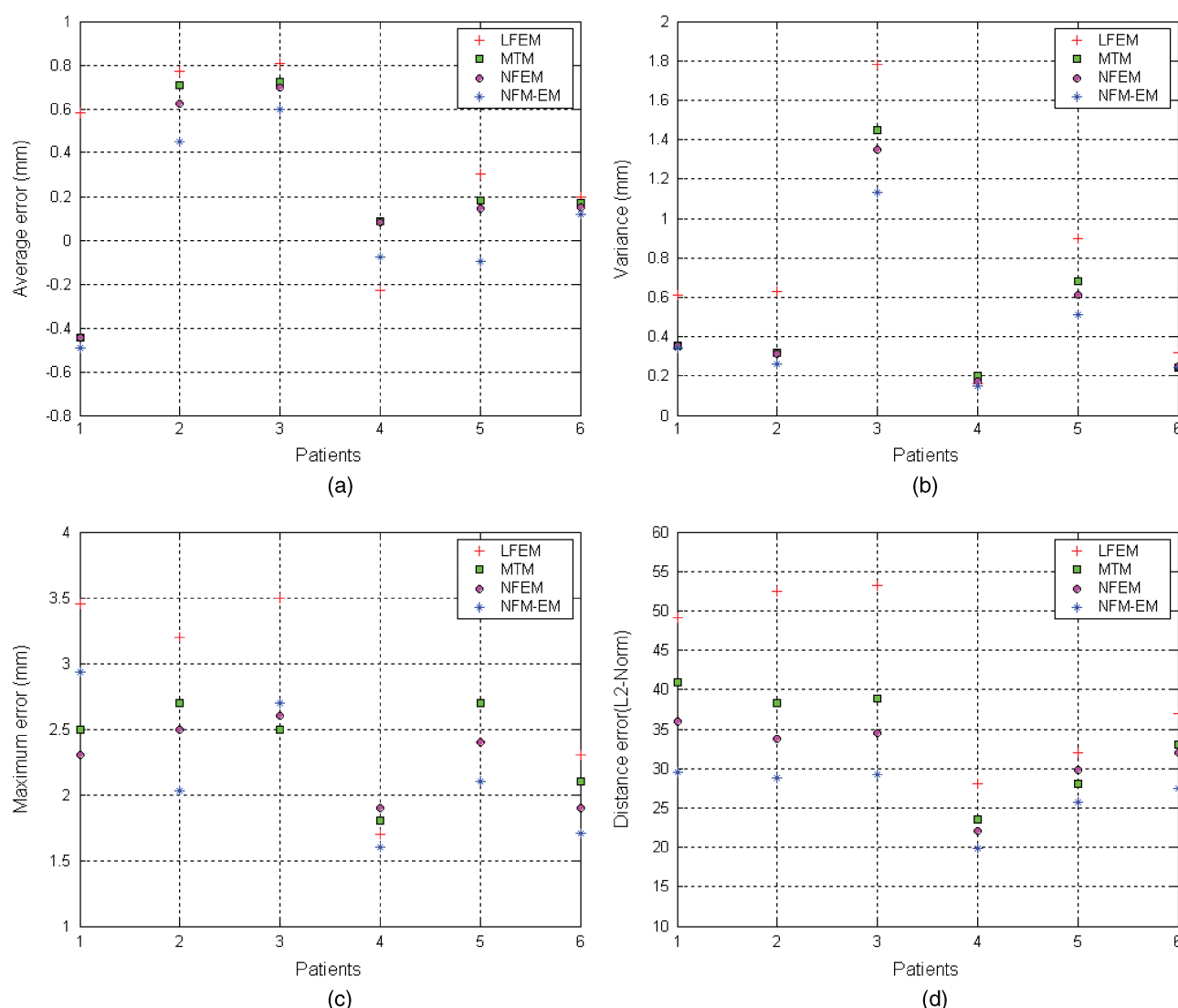


Figure 18. For six cases, quantitative validation results of the predictions calculated using four different models, consisting of: a linear finite element model (LFEM); a mass tensor model (MTM); a non-linear finite element model (NFEM); and the proposed method (NFM-EM). (a) Average errors; (b) variance; (c) maximum errors; (d) accumulated distance errors (L2-Norm)

postoperative CT scan. In addition, there are typical regions (nose and lips) with large errors, which result from at least two aspects. First, the nose and lips are different from the face in material properties. Second, the soft tissues of the nose and lips are not directly attached to the bone tissues, so that their external forces cannot be estimated accurately.

Furthermore, when we asked some plastic surgeons from Shanghai 9th People's Hospital to help us validate this simulator, they thought this simulator could provide relatively accurate results for the prediction of craniofacial surgery, but they had to do much interaction work and had to spend much time on using our simulator, since during the simulation they first had to reconstruct the special geometric model of the soft tissues using a manual segmentation and reconstruction method, and define the cut regions with the manual measurement method depending on the surgeon's experience. Second, in each step, it takes much computational time to compute the

biomechanical model. Therefore, they also expected the simulator described in the paper to be applied in the CSPS with less intervention and less computational time.

Nevertheless, the surgeons were satisfied with the robustness and accuracy of the NFM-EM, which are presented in the section on Performance evaluation.

Conclusion

This paper presents a novel method for assisting surgeons to automatically predict new facial configurations based on a pre-specified bone-related plan. An accurate collision detection method using the signed distance field is the key technique in automatically predicting the craniofacial surgery. It performs accurate contact handling between the bones and the soft tissues. When the bones move following a prespecified bone-related plan, this method can automatically and dynamically

detect the inter-penetration depth and the contact normals between the moved bones and the soft tissues. These inter-penetration depths and contact normals are needed for the biomechanical model of the soft tissues. Moreover, the signed distance field computation method is improved in both computational efficiency and memory requirements.

In addition, this work proposes an improved biomechanical model for enhancing accuracy and simulation realism required in the craniomaxillofacial surgical simulation. The approach estimates the optimal material parameters of the skin and internal tissues by investigating the hyperelastic model of the facial soft tissues. Moreover, a non-linear biomechanical model based on mixed elements is proposed, which better addresses the heterogeneity in geometry and material properties found in the soft tissues of the face. In the quantitative evaluation and the comparison, the variances of the distance errors are the least among all methods, which means that NFM-EM is the most stable model, and the L2 - Norm stays <30 mm, which is highly promising with respect to clinical standards. Therefore, this approach is particularly suited for craniomaxillofacial surgery simulation.

Nevertheless, the methods remain limited to the prediction of soft tissue deformation. The bone-related planning that effects the desired tissue deformation must still be developed by the surgeon. For future work, therefore, we will promote an approach for automatic design of bone remodelling plans based on direct specification (as opposed to simulation) of postoperative facial configurations.

Appendix A

C¹ shape functions for a plate-bending element

For a plate-bending element, the shape functions for the nine degree of freedom triangle are based on the Hermit interpolation functions and are as expressed as:

$$\omega_0 = \mathbf{N}^9(L_1, L_2, L_3)\mathbf{a}^e \quad (0.22)$$

$$\begin{aligned} \text{where } \mathbf{N}^9 &= [\mathbf{N}_1^9, \mathbf{N}_2^9, \mathbf{N}_3^9] \\ \text{and } \mathbf{N}_1^{9T} &= \begin{bmatrix} N_1 \\ N_{x1} \\ N_{x2} \end{bmatrix} \\ &= \begin{bmatrix} L_1 + L_1^2L_2 + L_1^2L_3 - L_1L_2^2 - L_1L_3^2 \\ b_2(L_3L_1^2 + \frac{1}{2}L_1L_2L_3) - b_3(L_1^2L_2 + \frac{1}{2}L_1L_2L_3) \\ c_2(L_3L_1^2 + \frac{1}{2}L_1L_2L_3) - c_3(L_1^2L_2 + \frac{1}{2}L_1L_2L_3) \end{bmatrix} \end{aligned}$$

Similarly, the shape functions for the second and third nodes can be exploited in terms of the symmetry of the triangle in barycentric coordinates. Namely, \mathbf{N}_2^{9T} and \mathbf{N}_3^{9T} are defined by taking in turn the subscripts of all the variables in \mathbf{N}_1^{9T} following the rules $1 \rightarrow 2 \rightarrow 3$ and $3 \rightarrow 1$.

In equation (0.22), although the surface is C¹-continuous at each mesh vertex and also within each patch, discontinuities occur at the middle of each edge of the triangle. In order to address this problem, Zienkiewicz (35) introduced further a set of three rational blend functions to control the cross-boundary derivatives. These three blend functions are defined as follows:

$$\begin{aligned} \varepsilon_{23} &= \frac{L_1L_2^2L_3^2(1+L_1)}{(L_1+L_2)(L_1+L_3)}, \quad \varepsilon_{31} = \frac{L_1^2L_2L_3^2(1+L_2)}{(L_2+L_3)(L_2+L_1)}, \\ \varepsilon_{12} &= \frac{L_1^2L_2^2L_3(1+L_3)}{(L_3+L_1)(L_3+L_2)} \end{aligned}$$

To obtain the C¹-continuous interpolation with nine degrees of freedom, we first need to compute the average of the corresponding cross-boundary derivatives at the endpoints of each edge for each of the nine components of \mathbf{N}^9 , defined as follows:

$$\begin{bmatrix} \left(\frac{\partial \omega_0}{\partial \bar{n}} \right)_{2,3}^a \\ \left(\frac{\partial \omega_0}{\partial \bar{n}} \right)_{3,1}^a \\ \left(\frac{\partial \omega_0}{\partial \bar{n}} \right)_{1,2}^a \end{bmatrix} = \mathbf{Y}\mathbf{a}^e$$

and the normal derivative at the edge midpoints defined as follows:

$$\begin{bmatrix} \left(\frac{\partial \omega_0}{\partial \bar{n}} \right)_{2,3} \\ \left(\frac{\partial \omega_0}{\partial \bar{n}} \right)_{3,1} \\ \left(\frac{\partial \omega_0}{\partial \bar{n}} \right)_{1,2} \end{bmatrix} = \mathbf{Z}\mathbf{a}^e$$

\mathbf{Y} and \mathbf{Z} are able to define nine interpolation functions with the three blend functions to feature the global C¹-continuity. Thus, the total C¹-continuous interpolation functions can be reformulated as follows:

$$\omega = \mathbf{N}^9\mathbf{a}^e + [\phi_{23} \ \phi_{31} \ \phi_{12}](\mathbf{Y} - \mathbf{Z})\mathbf{a}^e$$

where $\phi_{23} = \frac{\varepsilon_{23}}{(\partial \varepsilon_{23} / \partial n)_4}$, ϕ_{31} and ϕ_{12} are defined by taking in turn the subscripts of the ϕ_{23} .

Acknowledgements

The authors would like to thank the anonymous reviewers and editors for their comments and suggestions, which greatly helped to improve the quality of this study. The research was supported by a Shanghai Leading Academic Discipline Project (No. S30602) and the Shanghai Science Foundation of China (Grant No. 08ZR1409300). The authors would like to thank Professor Xiongzheng Mu and Dr Zheyuan Yu in the Shanghai 9th People's Hospital for their assistance in acquiring patients' datasets and validating the results.

Supporting Information on the Internet

The following supporting information may be found in the online version of this article:

Movie shows the results of the soft tissue deformation based on mixed-element modelling, and also shows the predicted results under different movements of the bones.

References

1. Terzopoulos D, Walters K. Physically-based facial modelling, analysis and animation. *Visualiz Comput Anim* 1990; **1**(4): 73–80.
2. Lee Y, Terzopoulos D, Walters K. Realistic modeling for facial animation. *Comput Graphics (Ann Conf Ser)* 1995; **29**: 55–62.
3. Koch RM, Gross MH, Carls FR, et al. Simulating facial surgery using finite element models. In *Proceedings of SIGGRAPH '96*. ACM Press: New Orleans, LA, 1996; 421–428.
4. Keeve E, Girod S, Pfeie P, et al. Anatomy-based facial tissue modeling using the finite element method. *Proceedings of IEEE Visualization '96*. IEEE Computer Society: San Francisco, CA, 1996; 21–28.
5. Bro-Nielsen M, Cotin S. Real-time volumetric deformable models for surgery simulation using finite elements and condensation. *Comput Graphics Forum* 1996; **15**(3): 57–77.
6. Cotin S, Delingette H, Ayache N. Real-time elastic deformations of soft tissues for surgery simulation. *IEEE Trans Visualiz Comput Graphics* 1999; **5**(1): 62–73.
7. Cotin S, Delingette H, Ayache N. A hybrid elastic model allowing real-time cutting, deformations and force-feedback for surgery training and simulation. *Visual Comput* 2000; **16**(8): 437–452.
8. Zhuang Y, Canny J. Haptic interactions with global deformations. In *IEEE International Conference on Robotics and Automation*, San Francisco, USA, 2000; 2428–2433.
9. Delingette H. Toward realistic soft-tissue modeling in medical simulation. *Proceedings of IEEE: Special Issue on Surgery Simulation*. *IEEE Comput Soc* 1998; 512–523.
10. Wu X, Downes M, Goktekin T, et al. Adaptive nonlinear finite elements for deformable body simulation using dynamic progressive meshes. In *Proceedings of Eurographics 2001*, Manchester, UK, 2001; 349–358.
11. Picinbono G, Delingette H, Ayache N. Non-linear and anisotropic elastic soft tissue models for medical simulation. In *IEEE International Conference on Robotics and Automation*, vol 2, Seoul, Korea, 2001; 1370–1375.
12. Picinbono G, Delingette H, Ayache N. Non-linear anisotropic elasticity for real-time surgery simulation. *Graph Models* 2003; **65**(5): 305–321.
13. Gladilin E, Zachow S, Deuhard P, et al. A biomechanical model for soft tissue simulation in craniofacial surgery. In *Proceedings of Medical Imaging and Augmented Reality*, 2001; 137–141.
14. Schwartz JM, Deniger M, Rancourt D, et al. Modeling liver tissue properties using a non-linear visco-elastic model for surgery simulation. *Med Image Anal* 2005; **2**: 103–112.
15. Sokhanvar S, Dargahi J, Packirisamy M. Hyperelastic modelling and parametric study of soft tissue embedded lump for misapplications. *Int J Med Robotics Comput Assist Surg* 2008; **4**(3): 232–241.
16. Chabanas M, Luboz V, Payan Y. Patient specific finite element model of the face soft tissues for computer-assisted maxillofacial surgery. *Med Image Anal* 2003; **7**: 131–151.
17. Chabanas M, Payan Y, Marecaux C, et al. Comparison of linear and non-linear soft tissue models with post-operative CT scan in maxillofacial surgery. In *Lecture Notes in Computer Science*. Springer: New York, 2004; 19–27.
18. Zachow S, Gladiline E, Hege HC, et al. Finite element simulation of soft tissue deformation. In *Proceedings of Computer Assisted Radiology and Surgery (CARS)*, San Francisco, USA, 2000; 23–28.
19. Westermarck A, Zachow S, Eppley B. Three-dimensional osteotomy planning in maxillofacial surgery including soft tissue prediction. *J Craniofac Surg* 2005; **16**(1): 100–104.
20. Mollemans W, Schutyser F, Nadjmi N, et al. Predicting soft tissue deformations for a maxillofacial surgery planning system: from computational strategies to a complete clinical validation. *Med Image Anal* 2007; **1**: 282–301.
21. Lombardo JC, Cani MP, Neyret F. Real-time collision detection for virtual surgery. *Proceedings of Computer Animation '99*. IEEE Computer Society: Geneva, Switzerland, 1999; 82–91.
22. Joshi B, Lee B, Popescu DC, et al. Multiple contact approach to collision modelling in surgical simulation. *Stud Health Technol Informat* 2005; **111**: 237–242.
23. Teschner M, Kimmeler S, Heidelberger B, et al. Collision detection for deformable objects. *Comput Graphics Forum* 2005; **24**(1): 61–81.
24. Li X, Gu L, Zhang S, et al. Hierarchical spatial hashing-based collision detection and hybrid collision response in a haptic surgery simulator. *Int J Med Robotics Comput Assist Surg* 2008; **4**(1): 77–86.
25. Fisher S, Lin M. Fast penetration depth estimation for elastic bodies using deformed distance fields. In *Proceedings of the 2001 IEEE/RSJ International Conference on Intelligent Robots and Systems*. IEEE Computer Society: Maui, HI, USA, 2001; 330–336.
26. Fuhrmann A, Sobottka G, Gross C. Distance fields for rapid collision detection in physically based modeling. In *International Conference on Computer Graphics and Vision '03*, Moscow, 2003; 58–65.
27. Frisken SF, Perry RN, Rockwood AP, et al. Adaptively sampled distance fields: a general representation of shape for computer graphics. In *Proceedings of the Special Interest Group on Computer Graphics and Interactive Techniques (SigGraph)* 2000; 249–254.
28. Baerentzen JA. Signed distance computation using the angle weighted pseudonormal. *IEEE Trans Visualiz Comput Graphics* 2005; **11**(3): 243–253.
29. Keeve E, Schaller S, Girod S, et al. Adaptive surface data compression. *Signal Process Med Image Compress* 1997; **59**(2): special issue): 211–220.
30. Paiva A, Lopes H, Lewiner T. Robust adaptive meshes for implicit surfaces. In *IEEE Proceedings of the XIX Brazilian Symposium on Computer Graphics and Image Processing (SIBGRAPI '06)*, 2006; 205–212.
31. Fung Y. *Biomechanics: Mechanical Properties of Living Tissue*. Springer: New York, 1993.
32. Natali A, Carniel E, Pavan P, et al. Hyperelastic models for the analysis of soft tissue mechanics: definition of constitutive parameters. In *First IEEE/RAS-EMBS International Conference on Biomedical Robotics and Biomechatronics*, Pisa, Italy, 2006; 188–191.
33. Kvistedal YA, Nielsen PMF. Investigating stress–strain properties of *in vivo* human skin using multiaxial. In *Proceedings of the 26th IEEE EMBS*. IEEE Computer Society: San Francisco, CA, 2004; 5096–5099.
34. Mollemans W, Schutyser F, Cleynenbreugel JV, et al. Fast soft tissue deformation with tetrahedral mass spring model for maxillofacial surgery planning systems. In *Lecture Notes in Computer Science*. Springer: New York, 2004; 371–379.
35. Zienkiewicz OC, Taylor RL. 2000; *The Finite Element Method*, Fifth Edition, Volume 1: The Basis. Oxford.